A UAV Classification System based on FMCW Radar Micro-Doppler Signature Analysis

Beom-Seok Oh[a], Xin Guo[b], Zhiping Lin[a,*]

[a]*School of Electrical and Electronic Engineering, Nanyang Technological University, 50 Nanyang Avenue, Singapore 639798*
[b]*Temasek Laboratories, Nanyang Technological University, 50 Nanyang Drive, Singapore 637553*

Abstract

Due to its small size, slow flying speed, and low flying altitude, classification of mini-sized unmanned aerial vehicles (UAVs) using a frequency-modulated continuous wave (FMCW) surveillance radar is a challenging task. This is because the FMCW radar echo signals are acquired at a short dwell time and thus contain limited information about targets. In this paper, we first analyze FMCW radar returns from various types of UAVs and non-UAV objects in terms of the micro-Doppler signature (m-DS) pattern. Based on the analysis results, we propose an effective and efficient UAV classification system using FMCW radar echo signals. The proposed system consists of five main parts namely, i) burst selection, ii) rule-based scan pruning, iii) the empirical mode decomposition based m-DS analysis and features extraction, iv) error counting minimization based class label estimation, and v) scan-to-scan filtering. Our experimental results on physically measured FMCW radar echo signals from several types of UAVs and non-UAV objects show that the proposed system consistently outperforms a commercial-off-the-shelf UAV classification system in terms of the classification accuracy.

Keywords: UAV Classification, Micro-Doppler Signature, Surveillance FMCW radar, Empirical Mode Decomposition

1. Introduction

During the past decade, the usage of mini-sized unmanned aerial vehicles (will be called UAVs hereafter) has been exponentially increased in terms of the number and variety of applications. Parcel delivery, filming and agriculture are among the representative applications to list just a few (Al-Kaff et al., 2018). Such useful UAVs, however, can be a threat to security sensitive areas such as military zones, country borders, prisons, etc. This is because the UAVs can be used for spying, reconnaissance or even for attack. Fast and accurate UAV detection and classification has thus been one of the active research topics in recent years.

Due to its capability of fast remote sensing regardless of weather, radar technologies have been commonly utilized in UAV detection and classification (Chen & Ling, 2001). Among the radar

*Corresponding author

Accepted version, Expert Systems With Applications

technologies, an unmodulated continuous wave (CW) Doppler radar has been the most popular choice because it can capture rich information about the target by having a long dwell time. Since the size and the flying speed of UAVs is small and slow, the rich information plays an important role towards a high classification accuracy. Particularly, the majority of the UAV classification methods reported in the literature is based on the CW radar signals (Molchanov et al., 2014b; Harmanny et al., 2015; Torvik et al., 2016; Ren & Jiang, 2017; Kim et al., 2017; Oh et al., 2018; Ma et al., 2018). However, since the CW radar cannot determine the target range from the radar, and also requires human intervention to face the radar towards targets, its usability in a surveillance system is limited.

A frequency modulated CW (FMCW) Doppler radar, which is a type of the CW Doppler radar, is a better option for a surveillance system than the unmodulated CW Doppler radar. The FMCW radar can determine the target range, and thus can locate its position without human intervention. It is worth noting here that, however, designing a UAV classification system using the FMCW radar returns is not trivial. On top of the weak return signals due to its small size and slow flying speed of UAVs, the time resolution of the FMCW surveillance radar returns is poor due to its short dwell time on targets. This implies that the existing micro-Doppler signature (m-DS) (Chen & Ling, 2001) analysis techniques for CW radar signals (e.g., the short-time Fourier transform (STFT) (Stankovic et al., 2014) based spectrogram analysis (Molchanov et al., 2014b; Harmanny et al., 2015; Ren & Jiang, 2017) or cepstrogram analysis (Harmanny et al., 2015)) cannot directly be applied to FMCW radar echo signals. Moreover, to the best of our knowledge, little has been reported in the literature on UAV classification using a FMCW surveillance radar.

In this paper, we propose an efficient and effective system for UAV classification using FMCW surveillance radar echo signals. The proposed system consists of five main parts (see Fig. 1) namely, i) burst(s) selection and normalization, ii) rule-based scan pruning, iii) the empirical mode decomposition (EMD) (Huang et al., 1998) based m-DS analysis and features extraction, iv) total error rate minimization (TER) (Toh & Eng, 2008) based classification, and v) scan-to-scan filtering. Since the EMD method can decompose signals regardless of the signal dimension, it is adopted to analyze the low-dimensional FMCW radar returns for the m-DS analysis. Both the rule-based scan pruning and scan-to-scan filtering functions are introduced to enhance the classification accuracy and efficiency. The proposed system is implemented on board a ground-based surveillance commercial-off-the-shelf radar (will be called COTSradar hereafter for simplicity) for real-time application. The proposed system is applied to those tracked targets formed by the COTSradar.

The main contributions of this work can be enumerated as follows:

- Proposal of an effective and efficient UAV classification system for a ground-based surveillance FMCW radar. To enhance the effectiveness and efficiency, two novel functions namely, rule-based scan pruning and scan-to-scan filtering are introduced.

- Provision of the m-DS analysis results on FMCW radar echo signals from fixed-wing UAVs, rotary-wing UAVs and non-UAV objects. The analysis results reveal that the m-DS pattern induced by fixed-wing UAVs is different from that of rotary-wing UAVs.

- Provision of extensive experimental results on physically measured FMCW radar echo sig-

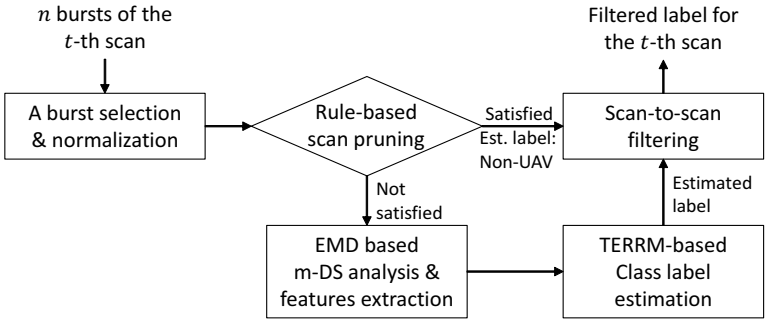

Figure 1: Five main parts of the proposed UAV classification system.

nals from various types of UAVs and non-UAV objects.

The remaining parts of this paper are organized as follows: a brief literature review on time-frequency analysis techniques for radar m-DS analysis is provided in Section 2. In Section 3, some background knowledge on the EMD and the TER methods are provided for immediate reference. We then provide our analysis results on FMCW radar echo signals from various types of UAVs and non-UAV objects in Section 4. Details of the proposed UAV classification system consisting of five main parts are provided in Section 5. Section 6 provides extensive empirical evaluation results on physically measured FMCW radar signals followed by some concluding remarks given in Section 7.

2. A brief literature review on time-frequency analysis methods used for the m-DS analysis

The radar m-DS induced by rotating blades of an aerial vehicle contains the unique characteristics of the aerial target. For example, several physical UAV parameters (e.g., the number of blades and its length, rotation rate of the rotor and blade tip velocity) can be retrieved from CW radar echo signals (Tahmoush, 2014; Harmanny et al., 2015; Oh et al., 2017). An effective analysis of the m-DS is thus a crucial step towards a high classification accuracy. In general, the m-DS analysis consists of two steps. Firstly, the m-DS is extracted by decomposing radar echo signals using a time-frequency analysis technique such as the STFT or its variation. The analysis results are then converted into a certain representation such as spectrogram, cepstrogram or cadence-velocity diagram (CVD) to signify the desired information to be extracted. Recall that the proposed system extracts the m-DS from FMCW echo signals using the EMD method with no further conversion into a representation.

The goal of this section is two-folded. Firstly, we briefly review the existing works on radar m-DS analysis and its classification in terms of their time-frequency analysis strategy. Table 1 provides a summary of the existing works. Note that those methods listed in Table 1 are selected due to their uniqueness in the time-frequency analysis and representation. Based on the literature review results, we then justify why the proposed system adopts the EMD method for the m-DS analysis under the given circumstances.

Table 1: A brief summary of the existing works on radar m-DS analysis and classification

Author (year)	Main objective / application	Time-frequency analysis for the m-DS extraction	Radar data
Kim et al. (2002)	Aircraft classification	Multiple signal classification (MUSIC)	CW
Stankovic et al. (2006a)	Separation of rigid body and micro-motion effects	STFT (Spectrogram) with order statistics	CW
Stankovic et al. (2006b)	Air target classification in heavy sea clutter	S-method by STFT with the Eigen decomposition	CW
Thayaparan et al. (2007)	Radar m-DS analysis	Wavelet transform & STFT (Spectrogram)	CW
Bai et al. (2008)	ISAR* imaging	Complex-valued EMD	CW
Björklund et al. (2012)	Gait classification	STFT (CVD)	CW
Du et al. (2013)	Aircraft classification	EMD with the CLEAN technique	CW
Molchanov et al. (2014a)	Aircraft classification	Bicoherence estimation based on STFT	CW
Harmanny et al. (2015)	UAV classification	STFT (Spectrogram, Cepstrogram)	CW
Wang et al. (2016)	Radar m-DS analysis	EMD or EEMD* with SPWVD*	CW
Tan et al. (2016)	Radar m-DS analysis	SPWVD Pre-Window	CW
Kim et al. (2017)	UAV classification	STFT (Spectrogram+CVD)	CW
Ren & Jiang (2017)	UAV detection	2D Complex-log spectrum based on STFT	CW
Oh et al. (2018)	UAV classification	EMD	CW
Li et al. (2017, 2019)	Active shooter detection	STFT (Spectrogram)	CW
Oh et al. (2019)	Blade flash decomposition	Augmented EMD	CW
Sun et al. (2019)	UAV detection	Iterative adaptive approach	FMCW

*Abbreviations: Inverse synthetic aperture radar (ISAR), Ensemble EMD (EEMD), Smoothed pseudo Wigner-Ville distribution (SPWVD).

It is observed from Table 1 that the majority of the works in the literature relies on the STFT. For example, Stankovic and his colleagues utilized the STFT together with the order statistics (Stankovic et al., 2006a) for ISAR imaging. They also proposed to use the S-method which was derived from the STFT together with the eigen decomposition (Stankovic et al., 2006b) for aerial target classification. The core idea of (Björklund et al., 2012; Harmanny et al., 2015; Kim et al., 2017; Li et al., 2017, 2019) is to explore into new features induced by the target objects by having several time-frequency representations such as CVD, spectrogram and cepstrogram. The authors of (Molchanov et al., 2014a; Ren & Jiang, 2017) proposed new time-frequency representations namely, the bicoherence estimation and the 2D complex-log spectrum derived using the standard STFT.

Although the STFT has been widely and successfully deployed in the m-DS analysis, it is well-known that its time-frequency resolution is relatively low. As an attempt to resolve this low resolution issue, the authors of (Kim et al., 2002; Tan et al., 2016; Sun et al., 2019) utilized high-resolution time-frequency analysis techniques such as the multiple signal classification (MUSIC) (Schmidt, 1986), the smoothed pseudo Wigner-Ville distribution (SPWVD) (Flandrin & Rioul, 1990) and the iterative adaptive approach (IAA) (Yardibi et al., 2010), respectively. With these alternatives, they achieved a high time-frequency resolution and thus a high classification accuracy.

However, these techniques are not appropriate for real-time classification of UAVs as they increase not only the time-frequency resolution but also the computational cost significantly compared to the STFT.

Another attempt made to resolve the low resolution issue was to decompose radar echo signals using the EMD method which is a non-Fourier-based time-frequency analysis technique (Bai et al., 2008; Du et al., 2013; Wang et al., 2016; Oh et al., 2018; Ma et al., 2018; Oh et al., 2019). By extracting discriminative features from a set of intrinsic mode functions which are obtained by the EMD method (see Section 3.1 for details), a better UAV classification accuracy than that of the Fourier-based approaches has been achieved (Oh et al., 2018). Moreover, the computational complexity of the standard EMD method appears reasonable to be executed in real-time applications (Fleureau et al., 2011).

Apart from the resolution issue, those Fourier-based prior arts require signals with a high sampling rate and/or a long dwell time. However, these two requirements are generally difficult to be satisfied in practical ground-based surveillance radar systems. For example, a surveillance radar scans a pre-defined sector (up to 360 degree) in a few seconds. This implies that the dwell time of the radar beam to any target object would be just a few tens of milliseconds, and thus the Doppler resolution obtained is quite limited. We note here that the dwell time of the FMCW radar utilized in this study (see Section 4.1 for details) is about 40ms which restricts the maximum coherent integration of 64 pulses. Thus, the Fourier-based time-frequency analysis methods cannot be deployed in this work. With these observations discussed above in mind, in this work, the standard EMD method is adopted for the m-DS analysis.

3. Preliminaries

In this section, a brief review of two methods namely, the EMD and the TER minimization for multi-category classification, is provided for immediate reference.

3.1. A brief review of the empirical mode decomposition (EMD)

The EMD method, which treats a signal as fast oscillations superimposed on slow oscillations, is an effective method for joint time-frequency analysis (Huang et al., 1998). The EMD decomposes a real-valued univariate signal $\boldsymbol{x} = [x_1, x_2, \cdots, x_d]^T \in \mathbb{R}^d$ into a set of oscillating waveforms centered at zero, called intrinsic mode functions (IMFs), as follows (Huang et al., 1998):

$$\boldsymbol{x} = \sum_{l=1}^{L} \boldsymbol{m}_l + \boldsymbol{q}_L, \tag{1}$$

where $\boldsymbol{m}_l$ denotes the l-th IMF and $\boldsymbol{q}_L$ is a residual function resulted after the L-th IMF is computed. Every IMF satisfies the following two conditions (Huang et al., 1998):

1. The number of local extrema (e.g., local minima and local maxima) and the number of zero-crossings are either equal or differ at most by one.
2. At any time point, the mean value of the envelope defined by the local maxima and the envelope defined by the local minima is zero.

Different from the Fourier transform, the basis function for EMD decomposition is not predefined. The EMD instead removes a lower frequency component locally from the input signal at each iteration till no more IMF can be derived from the residual. Such an adaptive decomposition process is called a "sifting process" in which the details can be found from (Huang et al., 1998).

Since the EMD method decomposes signals locally and adaptively, it is less sensitive to signal length d. The EMD method has been applied to various time series analysis problems such as speaker identification (Wu & Tsai, 2011), electroencephalography signal processing (Gaur et al., 2018) and financial time series analysis (Furlaneto et al., 2017; Zhou et al., 2019). Recently, the EMD has also successfully been applied to micro-Doppler radar target classification (Oh et al., 2017, 2018; Ma et al., 2018).

It is worth noting here that the EMD method suffers from several well-known issues such as the mode-mixing problem, the over sifting problem and the signal boundary issue. However, as shown in Fig. 1, the radar m-DS analysis is one of the five main components of the proposed system. By having the scan pruning step (see Section 5.2) and the scan-to-scan filtering step (see Section 5.4) which are designed to enhance the classification capability of the proposed system, possible errors caused by the EMD method can be compensated (see Section 6.5 for their impact in the classification accuracy). The proposed system shall be improved to handle these problems in our near future work.

3.2. A brief review of the total error rate (TER) minimization for multi-category classification

The TER of a binary-category classification system is the sum of the false acceptance rate (FAR) and the false rejection rate (FRR) as follows (Toh & Eng, 2008):

$$\text{TER} = \text{FAR} + \text{FRR} = \frac{1}{m^-}\sum_{i=1}^{m^-} L\left(g\left(\boldsymbol{x}_i^-\right) \geq \tau\right) + \frac{1}{m^+}\sum_{i=1}^{m^+} L\left(g\left(\boldsymbol{x}_i^+\right) < \tau\right), \tag{2}$$

where m^+ and m^- respectively indicate the positive class and the negative class population, $g(\cdot)$ denotes the predictor's output, τ is a predefined decision threshold, and $L(STATEMENT)$ is a step-loss function which returns a 1 whenever $STATEMENT$ is true, otherwise 0.

Let N_c be the total number of classes where each class represents a UAV model or an object type. Samples belonging to the c^{th}-category, $c = 1, \cdots, N_c$, are treated as in the positive class (denoted by a superscript '+') while all the other non-c^{th}-category samples are considered as in the negative class (denoted by a superscript '$-$'). With an appropriate normalization plus inclusion of an offset term η, minimization of the TER with respective to a classifier linear in its parameters $\boldsymbol{\alpha}_c$ turned out to have an analytic solution form (Toh & Eng, 2008):

$$\boldsymbol{\alpha}_c = \left(b\boldsymbol{I} + \boldsymbol{P}_c^T \boldsymbol{W}_c \boldsymbol{P}_c\right)^{-1} \boldsymbol{P}_c^T \boldsymbol{W}_c \boldsymbol{y}_c, \tag{3}$$

where $\boldsymbol{P}_c = \begin{bmatrix} \boldsymbol{P}_c^- \in \mathbb{R}^{m_c^- \times d'} \\ \boldsymbol{P}_c^+ \in \mathbb{R}^{m_c^+ \times d'} \end{bmatrix} \in \mathbb{R}^{m \times d'}$ is a regressor matrix, $\boldsymbol{y}_c = \begin{bmatrix} (\tau - \eta)\boldsymbol{1}^- \in \mathbb{N}^{m_c^-} \\ (\tau + \eta)\boldsymbol{1}^+ \in \mathbb{N}^{m_c^+} \end{bmatrix} \in \mathbb{N}^m$ is a target vector, m_c^- and m_c^+ $(m = m_c^- + m_c^+)$ respectively indicate the non-cth-class and the cth-class population sizes, $\boldsymbol{1}^- = [1, \cdots, 1]^T \in \mathbb{N}^{m_c^-}$ and $\boldsymbol{1}^+ = [1, \cdots, 1]^T \in \mathbb{N}^{m_c^+}$. Symbol $\boldsymbol{W}_c = \boldsymbol{W}_c^- + \boldsymbol{W}_c^+ \in \mathbb{R}^{m \times m}$ indicates a class-specific diagonal weighting matrix in which $\boldsymbol{W}_c^- = \text{diag}(1/m_c^-, \cdots, 1/m_c^-,$

$0,\cdots,0)$ and $\boldsymbol{W}_c^+ = \text{diag}\,(0,\cdots,0,1/m_c^+,\cdots,1/m_c^+)$, b is a regularization factor and $\boldsymbol{I}$ denotes an identity matrix with dimension matching that of $\boldsymbol{P}_c^T\boldsymbol{P}_c$.

4. FMCW radar micro-Doppler signature analysis of various target objects

As mentioned earlier in this paper, most of the radar-based UAV classification works reported in the literature have used radar signals acquired using a CW radar instead of a FMCW radar. The related literature thus lacks detailed analysis on FMCW radar echo from various types of UAVs as well as non-UAV objects. The goal of this section is to analyze the m-DS of FMCW radar echoes from various UAVs, and then observe how it is different from those of non-UAV objects. For UAVs, we analyze radar returns from both fixed-wing and rotary-wing types. As for the non-UAV objects, the radar echo signals from a walking person, vehicles, a UAV bird and a moving bicycle are investigated. Prior to providing our analysis results, some fundamental terminologies and definitions related to the FMCW radar utilized in our study will be briefly described in the following subsection.

4.1. The deployed FMCW radar and its terminologies

The COTSradar utilized in our UAV classification study is a ground-based surveillance radar which transmits linearly frequency modulated continuous waveforms in the frequency of X-band. Some parameters of the COTSradar are provided in Table 2. As shown in Fig. 2 (a), the COTSradar mechanically scans a preset sector repeatedly till the radar operation is terminated. Scanning from one bound (e.g., the left bound shown in Fig. 2 (a)) to the other bound (e.g., the right bound) is numbered with an increasing integer $t = 1,2,\cdots$. In each direction within a scan, the COTSradar transmits a certain number of pulses, which are called a burst and are processed coherently.

Table 2: Some parameters of the COTSradar

Operating frequency	X-band
Waveform	Linear frequency modulated continuous wave
Transmit power	Maximum 1 Watt
Typical detection range	Up to 5 km for rotary-wing UAV Up to 6 km for fixed-wing UAV Up to 13 km for pedestrian Up to 22 km for vehicle
Antenna scan speed	Either of 7°/s, 14°/s or 28°/s
Accuracy	Azimuth $\leq$ 5 milliradians Range (at 3 km range setting) $\leq$ 5 m
Weight	Radar sensor 18kg Operating Unit 4kg

Since the radar detection and tracking are beyond the scope of this work, our proposed UAV classification system shall only be applied to the radar tracks formed by the COTSradar (see part (a) of Fig. 6 for details). As shown in Fig. 2 (b), each radar track consists of scans which are all

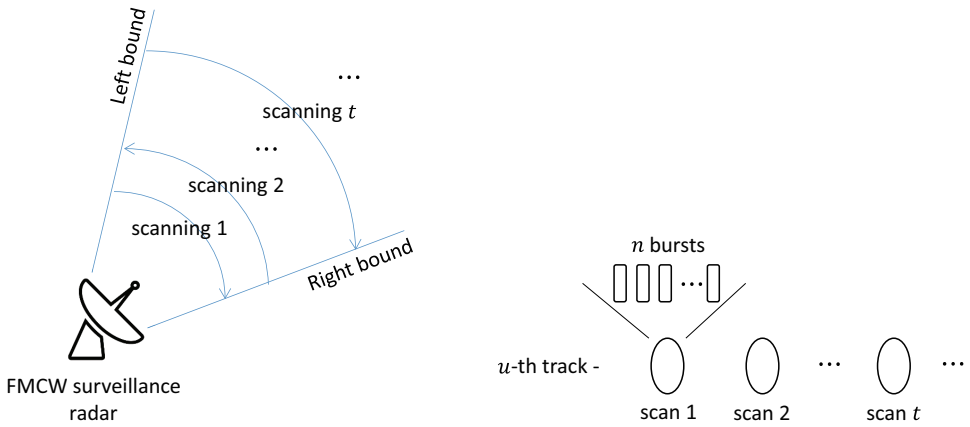

Figure 2: The COTSradar utilized in our study: (a) The mechanism of scanning and its numbering, and (b) definitions of a radar track formed by the COTSradar.

associated with a single radar target. Here, the radar target may or may not be a UAV. Fig. 2 (b) also shows that each scan consists of n number of bursts. Since the bursts of a scan are obtained at the t-th scanning, each scan is also numbered with the integer t. Note that the number of bursts n may vary over scans. Similar to that in (de Wit et al., 2012), we shall visualize a burst in a form of the range-velocity (RV) map generated using the fast Fourier transform (FFT). To suppress the Doppler sidelobe, the FFT is computed using the Hanning window. Moreover, we shall use both terminologies a burst and a RV map interchangeably hereafter unless otherwise specified.

4.2. Blade flash: the micro-Doppler signature induced by rotating blades

Blade flash is the phenomenon of radar m-DS induced by rotating blades (Molchanov et al., 2014b; Oh et al., 2017, 2018). According to (Oh et al., 2017), the blade flash contains the unique kinematics of UAVs, and thus could be the crucial information for classification. Due to space constraints, we refer to (Oh et al., 2017) for more details on the blade flash. In (Oh et al., 2017), the flash time T_f, which is a time gap between two adjacent blade flashes, in the time domain is defined as follows:

$$T_f = \frac{1}{N\Omega}, \tag{4}$$

where N denotes the number of blades and Ω indicates the rotation speed (round/sec) of the blades. In the frequency domain (e.g., in a RV map), the period of its spectrum peaks is defined as:

$$F_f = \frac{1}{T_f} = N\Omega. \tag{5}$$

This implies that the higher rotation speed Ω will produce a more discontinuous and periodical pattern in a RV map.

4.3. Micro-Doppler signature from a fixed-wing type UAV

Fig. 3 shows two RV maps which respectively contain radar echo from a fixed-wing UAV at different distances from the radar. In Fig. 3 (a), the body Doppler appears in the cell of 521m in

range and 7.7m/s in velocity. This means that the UAV at about 521m away from the radar, was receding into the distance at the velocity of 7.7m/s. The velocity will be a negative value if the target object approaches towards the radar. Besides the body Doppler, the m-DS induced by the rotating blades appears as a discrete and periodical pattern over the entire velocity axis. Except for the range cell of 521m, no such m-DS pattern is observed from other range cells.

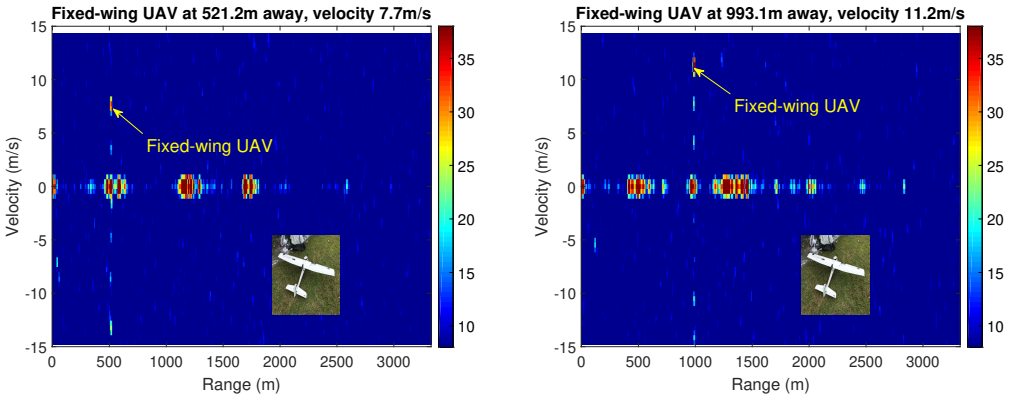

(a) (b)

Figure 3: Range-velocity map (in dB scale) of a fixed-wing UAV (model name: Firstar EX TW-757-K) at (a) 521.2m and (b) 993.1m away from the radar. Note that these RV maps are obtained using the FFT with the Hanning window while no zero-padding is considered.

To observe the effect of the target range on the strength of the m-DS, we now investigate into the RV map shown in Fig. 3 (b) which contains radar echo from the fixed-wing UAV at about 1000m away. Similar to Fig. 3 (a), both the body Doppler at the velocity of 11.2m/s and the m-DS appear clearly in the range cell of 993m. The body Doppler is stronger than that of the m-DS pattern which appears discrete and periodical over the velocity axis.

4.4. Micro-Doppler signature from rotary-wing type UAVs

Different from the fixed-wing type, rotary-wing type UAVs can further be divided into helicopter ($R = 2$), tricopter ($R = 3$), quadcopter ($R = 4$), hexacopter ($R = 6$) and octocopter ($R = 8$) according to the number of rotors, R. Among these rotary-wing UAVs, we shall explore into bursts returned from a helicopter (see Fig. 4 (a) and (b)), a quadcopter (see Fig. 4 (c) and (d)) and a hexacopter (see Fig. 4 (e) and (f)). Similar to the RV maps shown in Fig. 3, those bursts containing the target object at about 500m and 1000m away are investigated except for the helicopter model.

Fig. 4 (a), (c) and (e) respectively show RV maps containing radar echo from a helicopter (240m away from the radar), a quadcopter (524m away) and a hexacopter (497m away). Similar to the RV maps shown in Fig. 3, the body Doppler response again seems stronger than that of the m-DS. However, different from the fixed-wing UAV radar echo, the m-DS induced by these rotary-wing UAVs does not look like a discrete and periodical pattern. This is particularly due to the slower blades rotation speed than that of the fixed-wing UAV (see (5) for details). Moreover, since both quadcopter and hexacopter respectively have 4 and 6 rotors, the m-DS induced by each rotor with different initial angle are all combined into the return signal, and thus looks aperiodic.

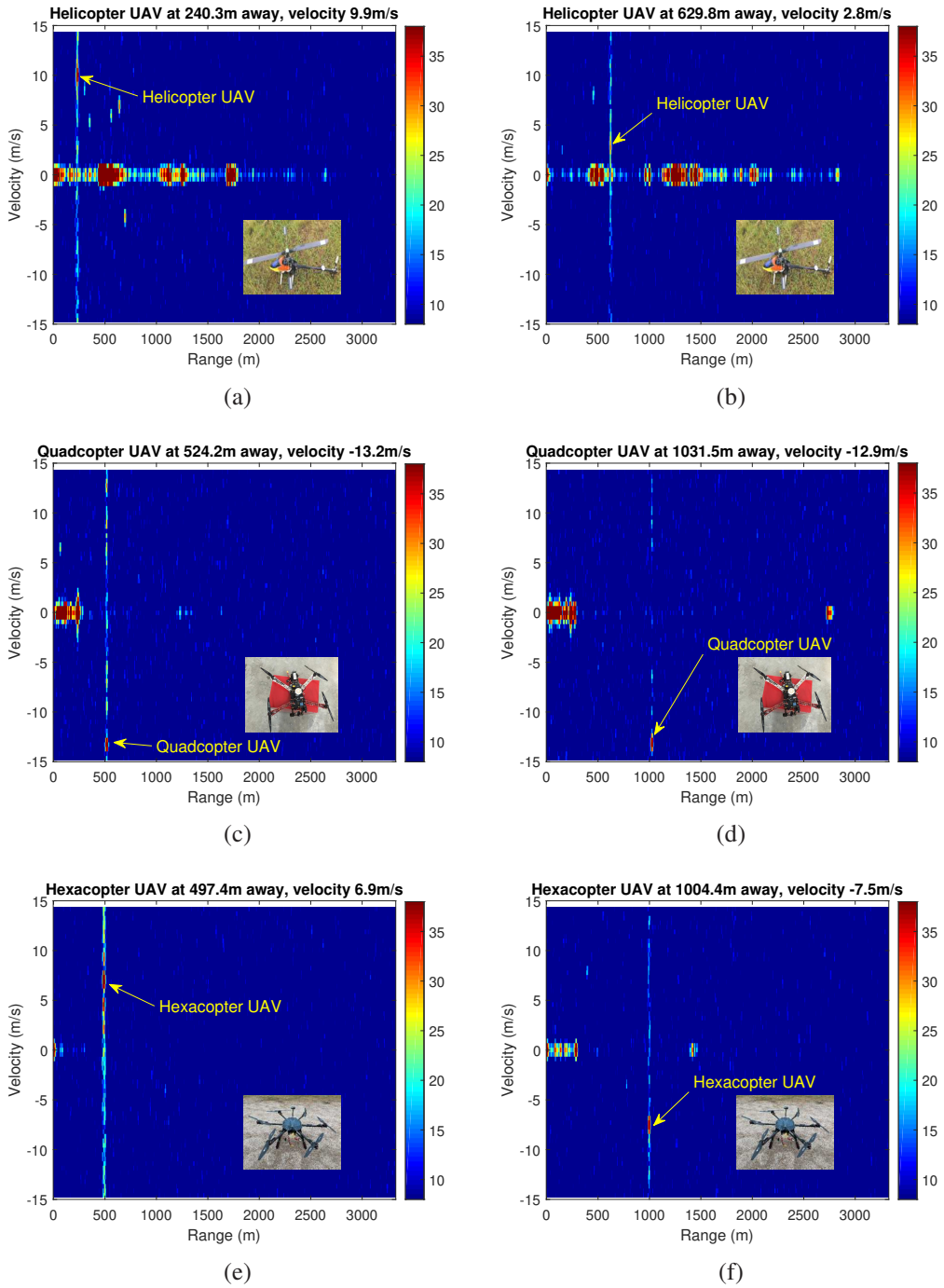

Figure 4: Range-velocity map (in dB scale) of rotary-wing UAVs. ((a) and (b)) Helicopter UAV at 240.3m and 629.8m away, ((c) and (d)) quadcopter UAV at 524.2m and 1031.5m away, and ((e) and (f)) hexacopter UAV at 497.4m and 1004.4m away from the radar. Note that these RV maps are obtained using the FFT with the Hanning window while no zero-padding is considered.

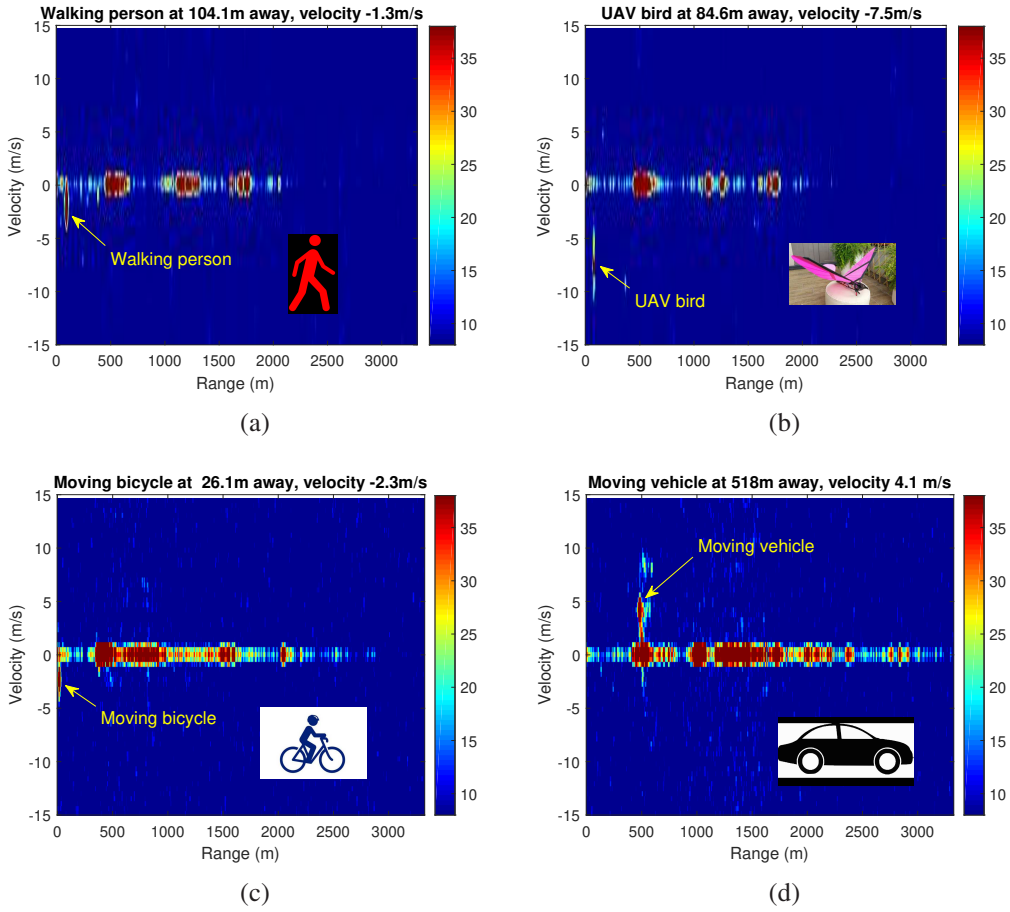

Figure 5: Range-velocity map (in dB scale) of non-UAV objects. (a) Walking person at 104.1m away, (b) UAV bird at 84.6m away, (c) moving bicycle at 26.1m away and (d) moving vehicle at 518m away from the radar. Note that these RV maps are obtained using the FFT with the Hanning window while no zero-padding is considered.

Similar to Fig. 3 (b), the RV maps shown in Fig. 4 (b), (d) and (f) contain radar echo from the three rotary-wing UAVs when they were at about 630m and 1000m away from the radar. Although the m-DS becomes weaker than that shown in Fig. 4 (a), (c) and (e), the m-DS can still be captured.

4.5. Micro-Doppler signature from non-UAV objects

We now investigate into RV maps shown in Fig. 5 which contain radar echo from (a) a walking person, (b) a flying UAV bird, a moving (c) bicycle and (d) vehicle, respectively. It is observed from Fig. 5 that no such blade flash effects appeared in Figs. 3 and 4, are induced by the investigated non-UAV objects. Even though the wheels on the bicycle and the vehicle were rotating, no m-DS was induced. This observation indicates that the m-DS induced by rotating blades contains enough information for discriminating UAVs from non-UAV objects.

4.6. Summary of observations

We have investigated into FMCW radar echo signals from a fixed-wing UAV, three rotary-wing UAVs and four non-UAV objects in terms of the m-DS (i.e., blade flash) effects. Our observations

can be summarized as follows:

- The m-DS induced by rotating blades appeared as a symmetrically spreading line (i.e., higher values in dB scale) over the entire velocity axis.
- The blade flash effects represented by an RV map became a discrete and periodic pattern if the blades rotation speed was high.
- The number of rotors affected the representation of the m-DS pattern. For example, the m-DS induced by a hexacopter (with $R = 6$ rotors) appeared to be stronger than that by a quadcopter (with $R = 4$ rotors).
- The investigated non-UAV objects (e.g., a walking person, a UAV bird, a moving bicycle and a moving vehicle) were observed to produce different m-DS patterns compared to that of the investigated UAVs.

5. Proposed UAV classification system for a surveillance FMCW radar

In this section, we propose an effective system for UAV classification using FMCW radar echo signals. The system is designed to discriminate UAVs from non-UAV targets (i.e., a two-category classification problem). The detected UAV can further be classified into the fixed-wing type and the rotary-wing type, which forms a three-category classification problem. Since, as aforementioned, the radar target detection and tracking are beyond the scope of this work, the proposed UAV classification system is only applied to the tracked targets formed by the COTSradar (see part (a) of Fig. 6). Note that the tracked targets may or may not be UAVs. The proposed system is then implemented on board the COTSradar for real-time classification.

As shown in part (b) of Fig. 6, n bursts $\{\boldsymbol{S}^u_{t,1}, \cdots, \boldsymbol{S}^u_{t,n}\}$ where $\forall \boldsymbol{S} = [\boldsymbol{s}_1, \boldsymbol{s}_2, \cdots, \boldsymbol{s}_{512}] \in \mathbb{C}^{64\times 512}$, of the t-th scan of the u-th track are input to the proposed system together with the range cell index $k_t \in \{1, \cdots, 512\}$. Note here that the 64 and 512 are the maximum number of the velocity and range cell indices, respectively. The proposed system starts with (Step 1) selecting the representative burst $\boldsymbol{S}^u_t$ among the n bursts followed by a signal normalization. The normalized burst $\widetilde{\boldsymbol{S}}^u_t$ is then (Step 2) evaluated by two simple rules checking the existence of the m-DS induced by a UAV. If any of the two rules is satisfied, the t-th scan is immediately regarded to be in the non-UAV class without further classification process. If the t-th scan survives from the rules, on the contrary, (Steps 3 and 4) its class label is then estimated by the proposed classification process. The estimated class labels are (Step 5) finally associated with the historical classification results within the track to stabilize the classification outcomes. Each of these five parts is described in the following subsection in greater detail.

5.1. Burst selection and normalization

As mentioned in Section 4.1, the number of bursts n of a scan varies over scans. Moreover, our preliminary investigation results shown in Fig. 7 reveal that the strength of the m-DS induced by rotating UAV blades also varies over bursts within a scan. For example, Fig. 7 shows six RV maps of a scan which contain radar echo from a helicopter UAV. Among the six RV maps, it is clear that

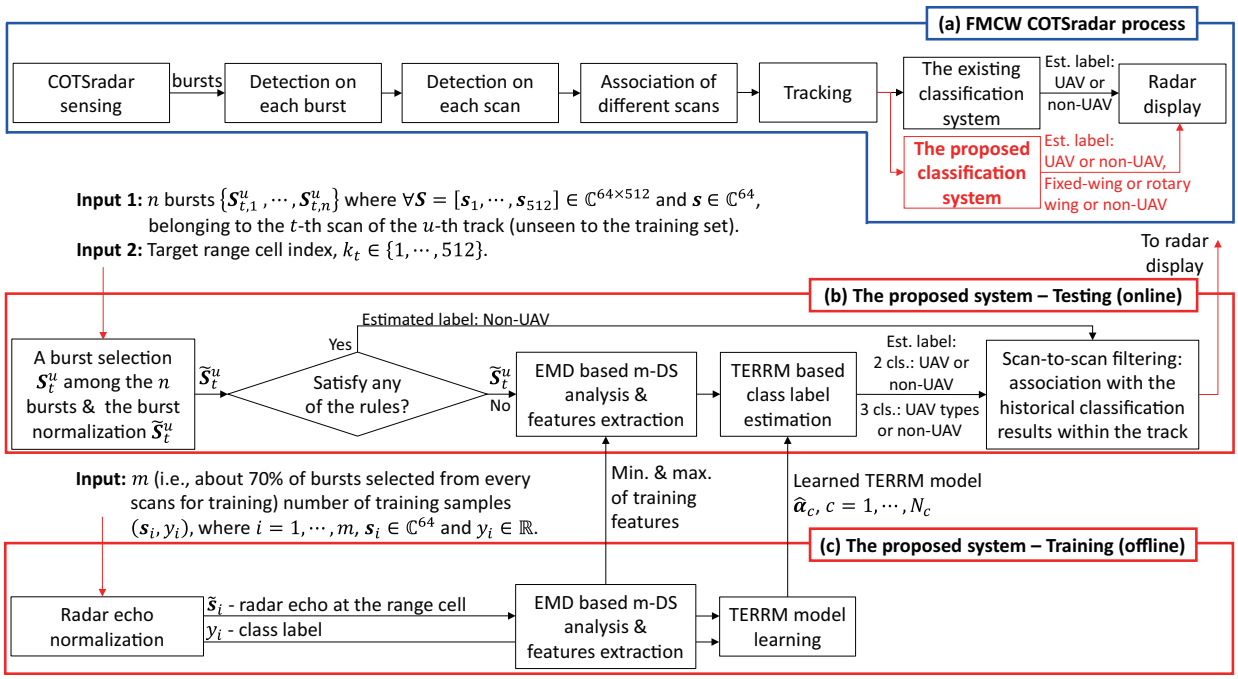

Note: Both the COTSradar classification method and the proposed classification method are to be executed in parallel for performance comparison. The number of bursts n of a scan may vary over scans.

Figure 6: The flow diagram of the COTSradar and the proposed UAV classification system.

the two bursts in the middle (Fig. 7 (c) and (d)) contain stronger m-DS than that of the other four bursts (Fig. 7 (a), (b), (e) and (f)).

With these observations in mind, in this work, we propose to use about 70% bursts of scans selected from the center (e.g., the bursts shown in Fig. 7 (b) to (e)) to train our classifier. In the online testing phase, only a single burst selected by $\lfloor \frac{n}{2} \rfloor + 1$ (e.g., Fig. 7 (d)) is used to represent the scan, and then for subsequent class label estimation. The selected bursts are then normalized as follows:

$$\widetilde{S}^u_t = \frac{Real(S^u_t)}{mean(|S^u_t|)} + j \cdot \frac{Imag(S^u_t)}{mean(|S^u_t|)}, \tag{6}$$

where $j = \sqrt{-1}$, $|\cdot|$ indicate the magnitude function, $mean(\cdot)$ denotes the mean function, $Real(\cdot)$ and $Imag(\cdot)$ respectively return the real part and the imaginary part of complex values.

5.2. Rule-based scan pruning

It is observed from Section 4 that the m-DS induced by rotating UAV blades appears as a vertically spreading line over the entire velocity axis in an RV map (see Figs. 3 and 4, for example). Since as shown in Fig. 5 no such m-DS pattern is triggered by non-UAV objects, its existence in an RV map could be a good indication to rule out those scans containing no UAVs. With these observations in mind, the following two simple rules are proposed:

- **Rule 1:** *Is the value of the target cell* $\hat{\mathbf{S}}^u_t(v, k_t)$ *strongest among the 7 adjacent range cells*

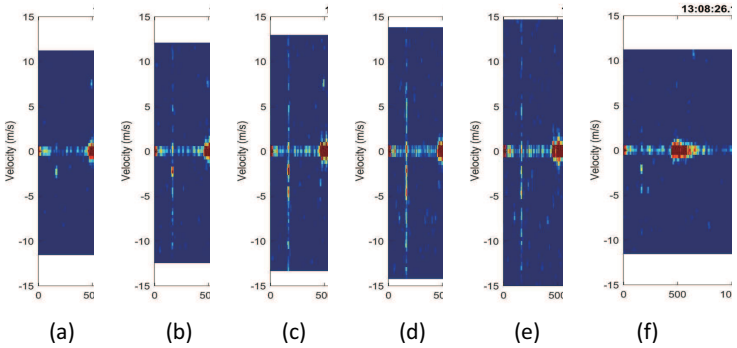

Figure 7: Six RV maps ((a)–(f)) belonging to a scan.

$\hat{\mathbf{S}}_t^u(v, k_t-3:k_t+3)$*? Here,* $\hat{\mathbf{S}}_t^u \in \mathbb{R}^{64\times 512}$ *is a normalized burst in dB scale from* $\widetilde{\mathbf{S}}_t^u$*,* $k_t \in \{1,\cdots,512\}$ *and* $v \in \{1,\cdots,64\}$ *respectively denote indices of the target range and velocity.*

- **Rule 2:** *Is the m-DS spreading over the entire velocity axis symmetrically? In a form of pseudocode, this rule can be written as: Is* $\max\left(\hat{\mathbf{S}}_t^u(1:15,k_t)\right) < 0.45$ && $\max\left(\hat{\mathbf{S}}_t^u(50:64,k_t)\right) < 0.45$*? where the '0.45' is an empirically chosen value.*

If any of these two rules is satisfied, the scan $\widetilde{\mathbf{S}}_t^u$ is immediately regarded as in the non-UAV class. Those scans survived from these two rules are then fed to the proposed UAV classification function for subsequent class label estimation as described in the following subsection.

5.3. m-DS analysis, features extraction and classification

The proposed UAV classification process consists of three main parts namely, i) the EMD-based m-DS analysis, ii) features extraction and normalization, and iii) the TER that adopts a reduced multivariate (TERRM) model based class label estimation. Details of each part are provided in the following subsections.

5.3.1. m-DS analysis using EMD method

As shown in part (c) of Fig. 6, let $\boldsymbol{s}_i \in \mathbb{C}^{64}$ where $i = 1,\cdots,m$, and m indicates the total number of training samples, denote the i-th radar signal for training. We note here that the radar signals $\boldsymbol{s}_i$ consist of complex values. Moreover, the signal resolution which is of 64 dimension, is not enough to draw meaningful information. To ease the data process while increasing its dimension, the complex-valued radar signals $\boldsymbol{s}_i$ are firstly converted to real-valued signals $\boldsymbol{x}_i$ as follows:

$$\boldsymbol{x}_i = [|\boldsymbol{s}_i|, Real(\boldsymbol{s}_i), Imag(\boldsymbol{s}_i)] \in \mathbb{R}^{(64\cdot 3)\times 1}. \tag{7}$$

The converted $\boldsymbol{x}_i$ are then respectively decomposed into L IMFs, $\boldsymbol{m}_l^i \in \mathbb{R}^{(64\cdot 3)\times 1}$, $l = 1,\cdots,L$ using the real-valued EMD method (see Section 3.1 for details). For simplicity, $\boldsymbol{m}_l^i$ will be denoted as $\boldsymbol{m}_l$ hereafter unless otherwise specified. Note that the number of resulted IMFs, L, varies according to the frequency contents contained in the signal $\boldsymbol{x}_i$. Moreover, our empirical analysis on UAV radar signals shows that the phenomenon of blade flashes is mainly captured by the first few IMFs. Based on these observations, only the first $K < L$ IMFs are used for features extraction.

5.3.2. Features extraction from IMFs, fusion and normalization

In this work, 13 geometrical and statistical features are proposed to be extracted from the first K IMFs. According to the extraction mechanism, the 13 features can be categorized into two types namely, i) features internally computed within individual IMFs and ii) features computed across two consecutive IMFs. The first type consists of 8 statistical or geometrical features while 5 geometrical ratio features belong to the second type. Among these 13 features, 8 features are taken from our previous works (Oh et al., 2018; Ma et al., 2018) while the remaining 5 features are newly proposed in this work.

(i) Features internally computed within individual IMFs. The 8 features belonging to this type consist of: 1) number of zero-crossing, 2) signal energy, 3) standard deviation, 4) normalized max-mean difference, 5) log energy entropy, 6) spectral energy density and 7) its maximum, and finally 8) distance between two frequency peaks. The first five features are computed in the time domain while the remaining three are computed in the frequency domain. The time domain features are described below in detail.

- *Feature 1*: Number of zero-crossing (Oh et al., 2018; Bai et al., 2008)

$$\boldsymbol{f}_{i,1} = [Z_1, Z_2, \cdots, Z_K]^T \in \mathbb{R}^K, \tag{8}$$

where

$$Z_l = \sum_{n=2}^{d} |sign[m_l(n)] - sign[m_l(n-1)]|, l = 1, \cdots, K,$$

$$sign[m_l(n)] = \begin{cases} 1 & \text{if} \quad m_l(n) \geq 0, \\ 0 & \text{if} \quad m_l(n) < 0, \end{cases} \text{ and } \boldsymbol{m}_l = [m_l(1), m_l(2), \cdots, m_l(d)].$$

- *Feature 2*: Normalized signal energy (Oh et al., 2018; Yu et al., 2006; Li et al., 2013)

$$\boldsymbol{f}_{i,2} = \left[\frac{E_1}{E}, \frac{E_2}{E}, \cdots, \frac{E_K}{E}\right]^T \in \mathbb{R}^K, \tag{9}$$

where $E_l = \sum_{n=1}^{d} |m_l(n)|^2$ denotes the signal energy of the l-th IMF, and $E = \sum_{l=1}^{K} E_l$.

- *Feature 3*: Standard deviation of IMFs (Oh et al., 2018)

$$\boldsymbol{f}_{i,3} = [std(\boldsymbol{m}_1), std(\boldsymbol{m}_2), \cdots, std(\boldsymbol{m}_K)]^T \in \mathbb{R}^K, \tag{10}$$

where $std(\cdot)$ indicates the standard deviation function.

- *Feature 4*: Normalized max-mean difference of IMFs (Oh et al., 2018)

$$\boldsymbol{f}_{i,4} = [D_1, D_2, \cdots, D_K] \in \mathbb{R}^K, \tag{11}$$

where

$$D_l = \frac{\max_\gamma(\boldsymbol{m}_l) - mean(\boldsymbol{m}_l > 0)}{\max_\gamma(\boldsymbol{m}_l)}, \; l = 1, \cdots, K,$$

and $\max_\gamma(\boldsymbol{m}_l)$ returns the γ-th maximum value of $\boldsymbol{m}_l$. The γ is to remove exceptional outliers such as pulse noises.

- *Feature 5*: Log energy entropy (Ma et al., 2018; Aydın et al., 2009)

$$\boldsymbol{f}_{i,5} = [En_1, En_2, \cdots, En_K]^T \in \mathbb{R}^K, \tag{12}$$

where $En = -\sum_{n=1}^{d} \left(\log_2 p\left(m_n\right)\right)^2$ and $p(m_n)$ indicates the probability mass function of $\boldsymbol{m}$.

Together with the above five time domain features, the following three features are extracted from the frequency domain.

- *Feature 6 & 7*: Spectral energy density and its maximum value

$$\boldsymbol{f}_{i,6} = [F_1, F_2, \cdots, F_K]^T \in \mathbb{R}^K, \tag{13}$$

$$\boldsymbol{f}_{i,7} = [\max\left(F_1\right), \max\left(F_2\right), \cdots, \max\left(F_K\right)]^T \in \mathbb{R}^K, \tag{14}$$

where

$$F_l = \sum_{t=-\infty}^{\infty} \left|M_l\left(f\right)\right|^2,\ l = 1, \cdots, K,$$

and $M_l\left(f\right)$ is the Fourier transform of $m_l(n)$.

- *Feature 8*: Distance between two frequency peaks (Oh et al., 2018)

$$\boldsymbol{f}_{i,8} = [P_1, P_2, \cdots, P_K]^T \in \mathbb{R}^K, \tag{15}$$

where

$$P_l = \frac{\left|\arg\max\left(F_l\right) - d/2\right| \times 2}{d},\ l = 1, \cdots, K.$$

As shown in equations (8)-(15), each feature vector is of dimension K.

(ii) Geometrical features computed across IMFs. As mentioned earlier in this subsection, five features are extracted across the first K IMFs namely, the ratio of 9) zero-crossing numbers, 10) signal energy, 11) spectral energy density, 12) maximum amplitude, and 13) the LogEn of two consecutive IMFs. Different from the first type features, these geometrical features are of dimension $K-1$ as described below:

- *Feature 9*: Ratio of the number of zero-crossing Z_l (8) (Oh et al., 2018)

$$\boldsymbol{f}_{i,9} = \left[\frac{Z_2}{Z_1}, \frac{Z_3}{Z_2}, \cdots, \frac{Z_K}{Z_{K-1}}\right]^T \in \mathbb{R}^{K-1}. \tag{16}$$

- *Feature 10*: Ratio of the signal energy E_l (9) (Bai et al., 2008; Yu et al., 2006)

$$\boldsymbol{f}_{i,10} = \left[\frac{E_2}{E_1}, \frac{E_3}{E_2}, \cdots, \frac{E_K}{E_{K-1}}\right]^T \in \mathbb{R}^{K-1}. \tag{17}$$

- *Feature 11*: Ratio of the spectral energy density F_l (13)

$$\boldsymbol{f}_{i,11} = \left[\frac{F_2}{F_1}, \frac{F_3}{F_2}, \cdots, \frac{F_K}{F_{K-1}}\right]^T \in \mathbb{R}^{K-1}. \tag{18}$$

- *Feature 12*: Ratio of the maximum amplitude $\max(\boldsymbol{m})$

$$\boldsymbol{f}_{i,12} = \left[\frac{\max(\boldsymbol{m}_2)}{\max(\boldsymbol{m}_1)}, \frac{\max(\boldsymbol{m}_3)}{\max(\boldsymbol{m}_2)}, \cdots, \frac{\max(\boldsymbol{m}_K)}{\max(\boldsymbol{m}_{K-1})}\right]^T \in \mathbb{R}^{K-1}. \tag{19}$$

- *Feature 13*: LogEn of two concatenated IMFs (Oh et al., 2018)

$$\boldsymbol{f}_{i,13} = \left[En\left(\boldsymbol{m}'_1\right), \cdots, En\left(\boldsymbol{m}'_{K-1}\right)\right]^T \in \mathbb{R}^{K-1}, \tag{20}$$

  where $\boldsymbol{m}'_l = \left[\boldsymbol{m}_l^T, \boldsymbol{m}_{l+1}^T\right]^T$ indicates a concatenation of two consecutive IMFs.

(iii) Features fusion and normalization. The extracted 13 feature vectors are subsequently fused at feature level via concatenation as follows:

$$\boldsymbol{f}_i = \left[\boldsymbol{f}_{i,1}^T, \boldsymbol{f}_{i,2}^T, \cdots, \boldsymbol{f}_{i,13}^T\right]^T \in \mathbb{R}^{13K-5}. \tag{21}$$

After the fusion, the i-th radar signal $\boldsymbol{x}_i \in \mathbb{R}^{(64\cdot 3)\times 1}$ is now represented by a feature vector $\boldsymbol{f}_i \in \mathbb{R}^{13K-5}$. The fused feature vectors extracted from the m training samples are subsequently stacked into a matrix form:

$$\boldsymbol{F} = [\boldsymbol{f}_1, \boldsymbol{f}_2, \cdots, \boldsymbol{f}_m] \in \mathbb{R}^{(13K-5)\times m}. \tag{22}$$

For the subsequent classification process, each row vector of $\boldsymbol{F}$ corresponding to a feature type is normalized to within the range of $[0,1]$ using the min-max normalization technique. Note that since the test data are not available beforehand, its features can only be normalized with respect to the minimum and maximum values of training features.

5.3.3. (Offline) Learning the category-specific TERRM model, $\hat{\boldsymbol{\alpha}}_c$

Recall that, as shown in equation (22), $\boldsymbol{F} = [\boldsymbol{f}_1, \boldsymbol{f}_2, \cdots, \boldsymbol{f}_m] \in \mathbb{R}^{(13K-5)\times m}$ is obtained after fusing the 13 feature vectors (21) followed by a min-max normalization. To enhance the discriminative power of the features, the feature vector $\boldsymbol{f}_i$, $i = 1, \cdots, m$, is expanded using the reduced multivariate (RM) polynomial model (Toh et al., 2004) giving rise to $\boldsymbol{p}(\boldsymbol{f}_i) \in \mathbb{R}^{d'}$. The RM expanded features are subsequently stacked up category-wise as follows:

$$\boldsymbol{P}_c^- = \begin{bmatrix} \boldsymbol{p}\left(\boldsymbol{f}_1^-\right), \\ \vdots \\ \boldsymbol{p}\left(\boldsymbol{f}_{m_c^-}^-\right) \end{bmatrix}_{m_c^- \times d'}, \quad \boldsymbol{P}_c^+ = \begin{bmatrix} \boldsymbol{p}\left(\boldsymbol{f}_1^+\right), \\ \vdots \\ \boldsymbol{p}\left(\boldsymbol{f}_{m_c^+}^+\right) \end{bmatrix}_{m_c^+ \times d'},$$

where $d' = 13K(2r-1) - 9r + 6$ and r indicates the polynomial order. With $\boldsymbol{P}_c^-$ and $\boldsymbol{P}_c^+$, the TER model parameter $\hat{\boldsymbol{\alpha}}_c$ can now be learned using equation (3).

5.3.4. (Online) Prediction of unseen test data

Let $\boldsymbol{f}_t \in \mathbb{R}^{13K-5}$ denotes a normalized feature vector (21) extracted from a test radar signal $\boldsymbol{x}_t = [|\boldsymbol{s}_t|, Real(\boldsymbol{s}_t), Imag(\boldsymbol{s}_t)] \in \mathbb{R}^{(64\cdot 3)\times 1}$. The prediction for a given test data $\boldsymbol{x}_t$ (unseen to the training data) can be computed using the learned TERRM model $\hat{\boldsymbol{\alpha}}_c$ (3) as follows:

$$\hat{\boldsymbol{y}}_t = \boldsymbol{p}(\boldsymbol{f}_t)^T [\hat{\boldsymbol{\alpha}}_1, \hat{\boldsymbol{\alpha}}_2, \cdots, \hat{\boldsymbol{\alpha}}_{N_c}],$$

where $\hat{\boldsymbol{y}}_t = [\hat{y}_1, \hat{y}_2, \cdots, \hat{y}_{N_c}]$ denotes the estimated model outputs over N_c classes, and $\boldsymbol{p}(\boldsymbol{f}_t) \in \mathbb{R}^{d'}$ denotes a RM expansion of $\boldsymbol{f}_t$. The *one-versus-all* technique is then used to predict the class label $\hat{c}$ for $\boldsymbol{x}_t$ as follows:

$$cls(\boldsymbol{x}_t) = arg\max_c \hat{\boldsymbol{y}}_t.$$

5.4. Scan-to-scan filtering within a radar track

As shown in part (b) of Fig. 6, the last step of the proposed system is to refine the estimated class label per scan based on the historical classification results within each track. Such process is also known as scan-to-scan association or scan-to-scan correction in the literature. The main objective of this refinement process is to prevent sudden changes in the classification outputs caused by weak radar return signal, detection error, tracking error, etc.

Fig. 8 illustrates the proposed scan-to-scan filtering function. As shown in the figure, the proposed classification system starts producing the estimated class label from the 4-th scan (i.e., $t \geq 4$). Particularly, a majority voting (see Line #28 of Algorithm 1) over the first four estimated labels $\hat{\boldsymbol{y}}^T(1, 1:4)$ is performed to estimate the class label for the 4-th scan. From the 5-th scan and onwards (see Lines #29–#34 of Algorithm 1), the estimated class label $\hat{\boldsymbol{y}}^T(1,t)$ is displayed if it is equivalent to the current display output y_{curr}. If the estimated label for the t-th scan $\hat{\boldsymbol{y}}^T(1,t)$ is different from that of y_{curr}, then another majority voting (see Line #32 of Algorithm 1) over the accumulated classification confidence values $\boldsymbol{\theta} \in \mathbb{R}^{1\times N_c}$ is conducted to estimate the class label.

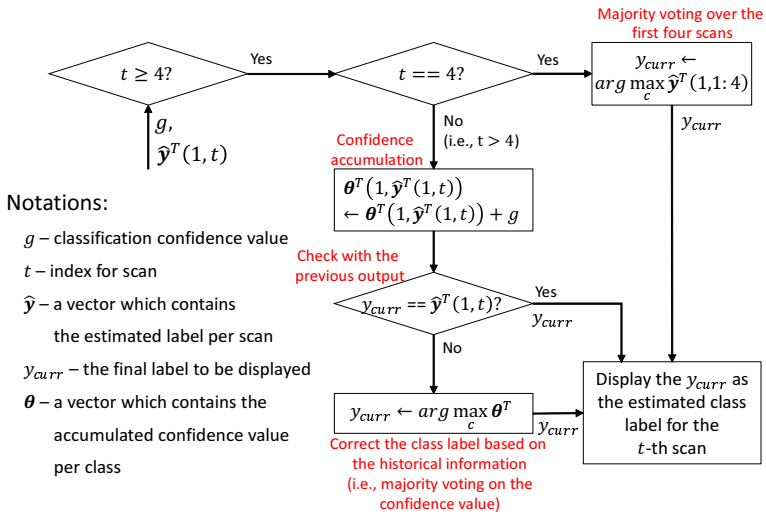

Figure 8: An illustrative description of the proposed scan-to-scan filtering method

We now take an example (see Fig. 9) to better describe the proposed scan-to-scan filtering process. As aforementioned, no estimated class label is produced for the first three scans. The estimated class label for the fourth scan is 'UAV' which is obtained by the majority voting over the first four scans (e.g., 3 UAVs and 1 non-UAV). The classification output is then displayed on the radar screen (i.e., $y_{curr} \leftarrow$ UAV). In this example, the obtained classification output for the fifth scan is 'non-UAV' which is different from the y_{curr}. When such a difference occurs, the proposed process refines the estimated classification label based on the accumulated confidence values.

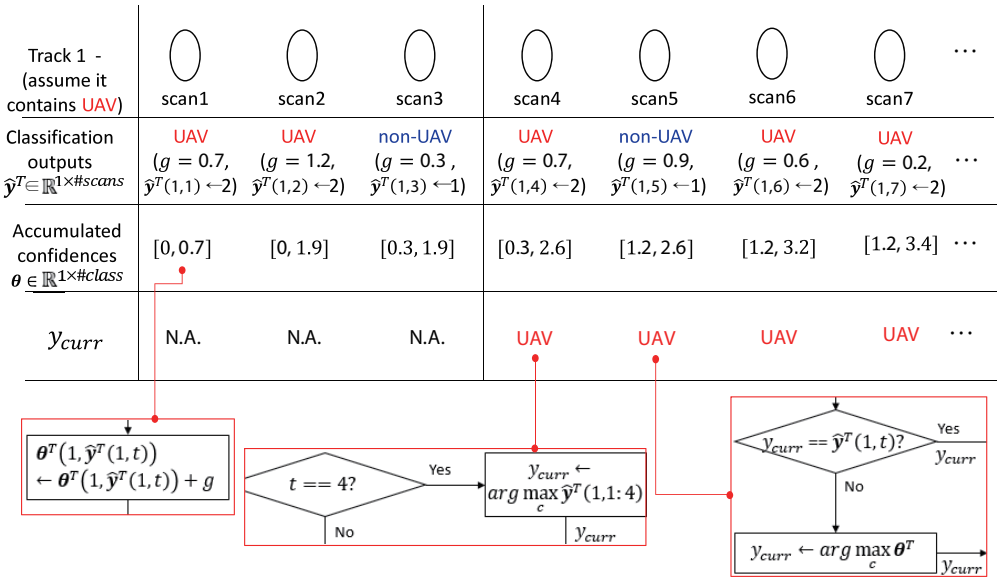

Figure 9: An illustrative example of the proposed scan-to-scan filtering

5.5. Summary of the proposed system

In the previous subsections, each of the 5 parts of the proposed UAV classification system are described. In order to provide an overview, the proposed system is summarized in Algorithm 1.

6. Experiments

In this section, the UAV classification performance of the proposed system is evaluated using physically measured FMCW radar signals. The FMCW radar echo signals from fixed-wing UAVs, rotary-wing UAVs and non-UAV objects, were collected using the COTSradar in six radar field trials. The data collected in the first three trials are used for training while the remaining data are used for test performance evaluation. To evaluate the proposed system under different aspects, four experiments are designed. The following subsections provide the details of our datasets, experimental setup and results together with our discussions.

6.1. (In-house) FMCW radar datasets of UAVs and Preprocessing

6.1.1. Radar field trials for data acquisition

The FMCW radar data of UAVs utilized in our experimental study has been collected in Singapore using the ground-based surveillance COTSradar (see Section 4.1 for specifications of the

Algorithm 1 The proposed UAV classification system (online testing phase)

Input 1: For the t-th scan of the u-th track, n number of bursts $\{\boldsymbol{S}_{t,1}^{u},\cdots,\boldsymbol{S}_{t,n}^{u}\}$, where $\forall \boldsymbol{S}=[\boldsymbol{s}_1,\cdots,\boldsymbol{s}_{512}] \in \mathbb{C}^{64\times 512}$ and $\forall \boldsymbol{s} \in \mathbb{C}^{64}$
Input 2: Target range cell index $k_t \in \{1,2,\cdots,512\}$
Input 3: The learned TERRM model $[\hat{\boldsymbol{\alpha}}_1,\cdots,\hat{\boldsymbol{\alpha}}_{N_c}] \in \mathbb{R}^{d'\times N_c}$ and RM polynomial order r
Input 4: EMD parameters (stopping criteria: 10 iterations, Spline interpolation)
Input 5: The min and max values of the training features $\boldsymbol{n}_{min}^{T} \in \mathbb{R}^{1\times(13K-5)}$ and $\boldsymbol{n}_{max}^{T} \in \mathbb{R}^{1\times(13K-5)}$
$g \in \mathbb{R} \leftarrow 0$ ▷ Initialization for classification confidence value
$\boldsymbol{\theta}^{T} \in \mathbb{R}^{1\times N_c} \leftarrow zeros(1,N_c)$ ▷ Initialization for confidence value accumulation
$\hat{\boldsymbol{y}}^{T} \in \mathbb{N}^{1\times 1000} \leftarrow zeros(1,1000)$ ▷ Initialization for the estimated class label
$y_{curr} \in \mathbb{R} \leftarrow 0$ ▷ Initialization for the final classification label
for $t \leftarrow 1,2,\cdots$ **do**
  $\boldsymbol{S}_t^{u} \in \mathbb{C}^{64\times 512} \leftarrow \boldsymbol{S}_{t,\lfloor \frac{n}{2} \rfloor+1}^{u}$ ▷ Burst selection
  $\widetilde{\boldsymbol{S}}_t^{u} \leftarrow \frac{Real(\boldsymbol{S}_t)}{mean(|\boldsymbol{S}_t^{u}|)} + j\frac{Imag(\boldsymbol{S}_t)}{mean(|\boldsymbol{S}_t^{u}|)}$
  if $\widetilde{\boldsymbol{S}}_t^{u}$ satisfies any of the two rules provided in Section 5.2 **then**
    $g \leftarrow 0.5$ ▷ Classification confidence value for those ruled-out scans is set to 0.5
    $\hat{\boldsymbol{y}}^{T}(1,t) \leftarrow cls(\text{non-UAV})$
  else
    $\widetilde{\boldsymbol{s}}_t \in \mathbb{C}^{64} \leftarrow \widetilde{\boldsymbol{S}}_{t,k_t}^{u}$ ▷ Micro-Doppler extraction from the k_t-th column of $\widetilde{\boldsymbol{S}}_t^{u}$
    $\boldsymbol{x}_t^{T} \in \mathbb{R}^{1\times 64\cdot 3} \leftarrow \left[Mag\left(\widetilde{\boldsymbol{s}}_t\right)^{T}, Real\left(\widetilde{\boldsymbol{s}}_t\right)^{T}, Imag\left(\widetilde{\boldsymbol{s}}_t\right)^{T}\right]$
    $\left[\boldsymbol{m}_1^{T},\cdots,\boldsymbol{m}_L^{T}\right]^{T} \in \mathbb{R}^{L\times 64\cdot 3} \leftarrow$ EMD($\boldsymbol{x}_t^{T}$, EMD parameters)
    $\boldsymbol{f}_t^{T} \in \mathbb{R}^{1\times 13K-5} \leftarrow$ Feature extraction$\left(\left[\boldsymbol{m}_1^{T},\cdots,\boldsymbol{m}_K^{T}\right]^{T}\right)$
    $\widetilde{\boldsymbol{f}}_t^{T} \leftarrow$Normalize $\boldsymbol{f}_t^{T}$ to fall into a range $[0,1]$ based on the given $\boldsymbol{n}_{min}^{T}$ and $\boldsymbol{n}_{max}^{T}$
    $\boldsymbol{p} \in \mathbb{R}^{d'} \leftarrow$ RMmodel$\left(\widetilde{\boldsymbol{f}}_t^{T}, r\right)$
    $\boldsymbol{o}^{T} \in \mathbb{R}^{1\times N_c} \leftarrow \boldsymbol{p}^{T}[\hat{\boldsymbol{\alpha}}_1,\cdots,\hat{\boldsymbol{\alpha}}_{N_c}]$
    $\hat{\boldsymbol{y}}^{T}(1,t) \leftarrow \arg\max_c \boldsymbol{o},\ c=1,\cdots,N_c$
    $g \leftarrow \max \boldsymbol{o}^{T}$
  end if
  if $t == 4$ **then**
    $y_{curr} \leftarrow \arg\max_c \hat{\boldsymbol{y}}^{T}(1,1:4)$
  else if $t > 4$ **then**
    $\boldsymbol{\theta}^{T}(1,\hat{\boldsymbol{y}}^{T}(1,t)) \leftarrow \boldsymbol{\theta}^{T}(1,\hat{\boldsymbol{y}}^{T}(1,t)) + g$
    if $y_{curr} \neq \hat{\boldsymbol{y}}^{T}(1,t)$ **then**
      $y_{curr} \leftarrow \arg\max_c \boldsymbol{\theta}^{T}$
    end if
  end if
end for

Note: 'A ← B' indicates that 'B' is assigned to 'A'.

radar). As shown in Table 3, the six radar field trials have been conducted over about 2 years. Note that all the six field trials were approved by Civil Aviation Authority of Singapore for flying UAVs, and by Info-communications Media Development Authority of Singapore for operating a radar system. For safety reasons, the UAVs were flown by licensed UAV pilots.

Table 3: Summary of six radar field trials conducted in Singapore. Note that radar signals acquired in the first three trials (Jun 2016, Jan 2017 and Feb 2017) are used for training while the remaining radar signals (acquired in Aug 2017, Oct 2017 and Mar 2018) are used for test performance evaluation.

Date	Place	UAVs types (number of UAV flying/data acquisition)	Flying details
Jun 2016	Open field	Fixed-wing (1), quadcopter (7), hexacopter (5), others[1] (5)	D[2]: 0.5km, A[3]: 60m
Jan 2017		Fixed-wing (6), helicopter (1), quadcopter (4), others[1] (1)	D: 1km, A: 60m
Feb 2017		Fixed-wing (13), helicopter (4), quadcopter (8)	D: 1km, A: 60m
Aug 2017		Fixed-wing (6), helicopter (3), quadcopter (3)	D: 1km, A: 60m
Oct 2017	Sea shore	Fixed-wing (6), quadcopter (5)	D: 2km, A: 60m
Mar 2018		Fixed-wing (2), hexacopter (2)	D: 3km, A: 120m

Note: [1]The 'others' include walking person, moving bicycle, UAV bird etc., [2]the maximum Distance between the COTSradar and the target UAV, [3]the maximum UAV flying Altitude.

As shown in Table 3, the first four field trials were conducted in an open field of rectangle shape where the diagonal length was about 1km. The COTSradar was placed in a corner of the field and UAVs were flown up to 1km away from the radar at about 60m altitude. The last two field trials were conducted in a sea shore area, where the direct distance from the radar to the shortest shoreline was about 300m, to fly UAVs for a longer distance (up to 3km) and at a higher altitude (up to 120m). The third column of Table 3 shows the types of UAVs adopted in each field trial where the number within the parentheses indicates the number of UAV flying (i.e., radar data acquisition).

6.1.2. Preprocessing and datasets partitioning

Recall that the main goal of this work is to design a UAV classification system. To stay focused only on the classification task, the existing radar detection and tracking functions of the COTSradar are utilized to form radar target candidates for classification (see part (a) of Fig. 6). However, our preliminary results revealed that the adopted COTSradar functions cause some errors in both detection and tracking. To minimize effects caused by those errors, all the acquired radar data are manually checked and corrected. We also form the groundtruth for classification based on the manual checking results.

The preprocessed data is then divided into two subsets namely, a training set and a test set. The training set consists of data acquired in the first three field trials (Jun 2016, Jan 2017 and Feb 2017 shown in Table 3). For the test set, those radar data acquired in the last three field trials (Aug 2017, Oct 2017 and Mar 2018) are utilized. Note that the test data, except for the data acquired in the Aug 2017 trial, were acquired under different environment compared to that of the training data. Table 4 provides a summary of the constructed datasets in terms of the data statistics. Since we have selected about 70% of bursts from each scan for training (see Section 5.1 for details), both

the number of bursts and scans are provided for the training set. For the test set in which only one single burst per scan is selected and used for classification, we provide only the number of scans.

Table 4: Specification of the radar data used for training and test accuracy evaluation

Data used for training		Data used for test accuracy evaluation	
Model	Number of bursts (scans)	Model	Number of scans
Non-UAV	7,667 (4,037)	Non-UAV	2,722
Fixed-wing UAV	1,964 (929)	Fixed-wing UAV	1,198
Helicopter UAV	1,491 (637)	Helicopter UAV	388
Quadcopter UAV	2,549 (1,041)	Quadcopter UAV	310
Hexacopter UAV	365 (145)	Hexacopter UAV	1,426

6.2. Experimental setup

6.2.1. Parameters setting and Protocols

The proposed system has two adjustable parameters namely, the number of IMFs K and the polynomial order r. From our previous study (Oh et al., 2018) in which CW radar returns from UAVs were analyzed using the EMD method for classification, the K was observed to be closely related to the classification accuracy. For example, the better classification accuracy was obtained at a higher value setting for K than that of a low value setting (Oh et al., 2018). However, due to its low signal dimension (e.g., $\boldsymbol{x} \in \mathbb{R}^{192}$), only up to $K = 3$ IMFs can be commonly extracted from the entire FMCW radar signals. Based on this observation, the K is fixed to 3 hereafter to maximize the classification accuracy. Different from the K, various polynomial orders $r \in \{1, 2, \cdots, 5\}$ shall be evaluated to observe its effect on the classification accuracy. Following (Toh, 2008), fixed threshold $\tau = 1$, offset $\eta = 0$ and bias $b = 1e-4$ settings are used for learning the TER model. The stopping criterion for the EMD sifting process is set to 10 iterations.

The first and third columns of Table 4 show that our data consists of radar returns from 4 types of UAVs and non-UAV objects. Here, the non-UAV objects include walking person, moving vehicle and bicycle, flying UAV bird etc. Though our data consists of 5 categories, knowing the specific UAV type is meaningless in a surveillance scenario. Moreover, our training data is imbalanced in terms of the number of samples. In this work, we thus shall focus only on either a two-category classification problem ('non-UAV' vs. 'UAV') or a three-category classification problem ('non-UAV' vs. 'rotary-wing UAV' vs. 'fixed-wing UAV'). The test accuracy is computed as follows:

$$\text{Test accuracy}(\%) = \frac{\text{Number of correctly matched test scans}}{\text{Total number of test scans}} \times 100.$$

All experiments were performed on a PC of 3.4GHz CPU with 16G RAM under Matlab platform (The MathWorks, 2019).

6.2.2. Evaluation scenarios

Table 5 shows that four experiments are designed and conducted to verify the accuracy of the proposed UAV classification system. In the first experiment (denoted as Experiment I in Table 5), the effectiveness of the extracted 13 features (see Section 5.3.2) is investigated in terms of the classification accuracy. Particularly, the impact of the newly included 5 features on top of the 8 features adopted from (Oh et al., 2018; Ma et al., 2018) is empirically investigated. The goal of Experiment II is to show the usefulness of the TERRM model over other classification methods. Both the classification accuracy and CPU processing speed elapsed for learning of the TERRM model are compared to these of the support vector machine (SVM) (Duda et al., 2012) that adopts either the linear kernel (SVM-Linear) or the radial basis function kernel (SVM-RBF).

Table 5: Four experiments for performance evaluation and comaprison

Index	Brief description	Rule-based scan pruning	Scan-to-scan filtering
Experiment I	Evaluation of the utilized 13 features	No	No
Experiment II	Evaluation of the adopted TERRM classifier	No	No
Experiment III	Evaluation of the proposed classification components	Yes / No	Yes / No
Experiment IV	Comparison with the COTSradar classification system	Yes	Yes

Under Experiment III, the impact of the proposed pre- and post-classification functions namely, the rule-based scan pruning (see Section 5.2) and the scan-to-scan filtering (see Section 5.4) are empirically evaluated. Particularly, we measure the classification accuracy of the proposed system with and without the two functions. Lastly, under Experiment IV, the best classification accuracy of the proposed UAV classification system is compared with that of the COTSradar classification system. The classification accuracies of the two methods are then subsequently analyzed in terms of the confusion matrix.

6.3. Experiment I: Evaluation of the utilized features

Among the 13 features proposed to be extracted from the first $K = 3$ IMFs, 8 features (e.g., *Features 1-5, 8, 9,* and *13*) are adopted from our previous works (Oh et al., 2018; Ma et al., 2018). The remaining 5 features (e.g., *Features 6, 7, 10-12*) are newly included in this work with an aim of improving the classification accuracy without increasing the computational cost. To verify the impact of the 5 features, as shown in Table 6, the classification accuracy obtained using the 8 features (Oh et al., 2018) is compared with that of using the entire 13 features. To evaluate the information contained in the features, both the rule-based scan pruning and the scan-to-scan filtering are disabled in this experiment.

From Table 6, the 5 new features appear to be helpful in improving the classification accuracy. Though the increment in accuracy is not very significant, the TERRM model trained using the 13 features consistently outperforms that of using the 8 features over the evaluated RM orders $r \in \{1, 2, \cdots, 5\}$ and the number of classes $\in \{2, 3\}$. Particularly, 0.05–0.71% for 2 class problem and 1.05–1.31% for 3 class problem have been improved.

Table 6: Test classification accuracy (%) comparison between using the 8 features taken from (Oh et al., 2018; Ma et al., 2018) and the entire 13 features.

No. of classes	Utilized features	RM polynomial order, r					Average % over r
		1	2	3	4	5	
2	8 features (Oh et al., 2018)	78.13	77.40	77.33	76.94	76.82	77.32
	13 features	78.18	77.66	77.55	77.30	77.53	77.64
3	8 features (Oh et al., 2018)	63.39	64.46	64.56	64.59	64.38	64.28
	13 features	64.44	65.69	65.77	65.90	65.62	65.48

6.4. Experiment II: Evaluation of the TERRM classifier

As shown in Table 5, this second experiment aims at verifying the usefulness of the adopted TERRM model for UAV classification. Particularly, the classification accuracy and the learning efficiency of the TERRM model will be compared with these of the SVM-Linear and the SVM-RBF model. Similar to Experiment I, both rule-based scan pruning and scan-to-scan filtering functions are disabled. Fig. 10 (a) and (b) respectively show the obtained classification accuracies (%) of TERRM, SVM-Linear and SVM-RBF and their learning speed in CPU processing time (sec). The performances of the TERRM and the SVM-RBF are respectively obtained over RM orders $r \in \{1,2,\cdots,5\}$ and RBF kernel widths $\in \{5,15,50,100,150\}$ which are selected from $\{0.1,1,5:2:19,50,80:10:150\}$. Since the SVM-Linear is not affected by r and kernel width, its performance is drawn as a line in Fig. 10 for easy comparison.

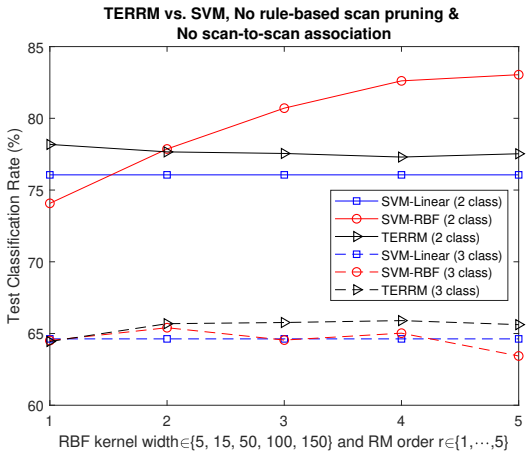

(a) Test classification accuracy (%)

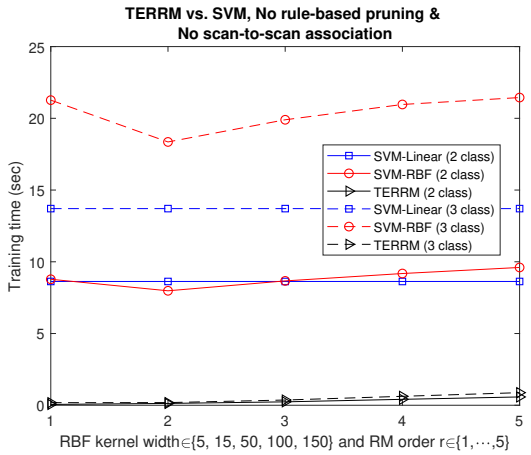

(b) CPU processing time (sec) elapsed for learning

Figure 10: (a) Test classification accuracy (%) and (b) CPU processing time (sec) performances obtained using the TERRM (plotted over RM orders $r \in \{1,2,\cdots,5\}$), the SVM-Linear and the SVM-RBF (plotted over RBF kernel width $\in \{5,15,50,100,150\}$). The SVM-Linear result is plotted as a line for easy comparison.

Fig. 10 (a) shows that the obtained accuracy values of the 2-category classification are higher than those of the 3-category classification. This implies the 3-category classification problem

is more difficult than that of the 2-category classification. Among the compared classifiers, the TERRM model consistently outperforms the SVM-Linear in terms of the test classification accuracy. The SVM-RBF outperforms the TERRM (particularly at RBF kernel widths $\in \{50, 100, 150\}$) under 2-category classification problem. However, the TERRM produces similar or even higher accuracy values under 3-category classification problem. Different from the accuracy performance, the TERRM model significantly outperforms the SVMs in terms of the learning efficiency as shown in 10 (b).

6.5. Experiment III: Evaluation of the proposed classification components

In this experiment, we now evaluate the impact of the rule-based scan pruning function and the scan-to-scan filtering function on the classification accuracy. Particularly, as shown in the first two columns of Table 7, different combinations of the two functions are respectively evaluated in terms of the test classification accuracy over RM orders $r \in \{1, 2, \cdots, 5\}$. For example, 'Yes' in the first two columns of Table 7 means that the indicated function is enabled, otherwise it is indicated by 'No'. The two 'No's shown in the third row of Table 7 means only the TERRM-based classification is performed. Each combination will be denoted by a pair within a parentheses (e.g., ('No', 'No') for the two 'No's discussed above) hereafter for convenience. Tables 7 and 8 respectively show the results obtained under the 2-category and 3-category classification problems.

Table 7: Test classification accuracy (%) obtained at different combinations of the proposed functions under the 2-category (non-UAV vs. UAV) classification problem.

Rule-based scan pruning	Scan-to-scan filtering	RM polynomial order r					Average % over r
		1	2	3	4	5	
No	No	78.18	77.66	77.55	77.30	77.53	77.64
Yes	No	76.39	76.06	76.08	75.83	75.88	76.05
No	Yes	91.69	91.61	91.46	91.46	91.83	91.61
Yes	Yes	93.99	94.39	94.24	94.26	94.26	94.23

It is observed from Table 7 that both the proposed functions play an important role in enhancing the classification capability of the proposed system. Particularly, the proposed system at a combination ('Yes', 'Yes') achieves the best test classification accuracy which is about 16.6% higher than that of ('No', 'No'). The combination ('No', 'Yes') produces about 14% higher accuracy value than that of ('No', 'No'). However, the combination ('Yes', 'No') produces about 1.6% lower accuracy than that of ('No', 'No'). This indicates that when the rule-based scan pruning function is enabled alone, it deteriorates the classification accuracy of the system. However, the accuracy comparison between ('No', 'Yes') and ('Yes', 'Yes') clearly shows that the rule-based scan pruning function helps in enhancing the classification capability when it is utilized together with the scan-to-scan filtering function.

Table 8 shows the test classification accuracies of the proposed system evaluated under the 3-category classification problem. Similar to Table 7, the proposed system produces the best classification accuracy at ('Yes', 'Yes'). From the accuracy comparison between combinations ('No', 'No') and ('No', 'Yes'), the scan-to-scan filtering function is observed to play an important

role in enhancing the classification accuracy. Table 8 also shows that, different from the results shown in Table 7, the combination ('Yes', 'No') produces about 2% higher accuracy than that of ('No', 'No').

Table 8: Test classification accuracy (%) obtained at different combinations of the proposed functions under the 3-category (non-UAV vs. fixed-wing UAV vs. rotary-wing UAV) classification problem.

Rule-based scan pruning	Scan-to-scan filtering	RM polynomial order r					Average over r
		1	2	3	4	5	
No	No	64.44	65.68	65.77	65.90	65.62	65.48
Yes	No	67.32	67.80	67.77	67.80	67.49	67.64
No	Yes	82.31	84.96	85.56	85.72	85.46	84.80
Yes	Yes	87.82	90.59	90.57	90.70	90.27	89.99

6.6. Experiment IV: Comparison with the COTSradar classification system

The test classification accuracy of the proposed system is now compared with that of the COTSradar classification system. Different from the proposed system, the COTSradar can only classify the detected target into either UAV or non-UAV categories. The accuracy comparison shall thus be conducted under the 2-category classification problem only. It is also noted here that the COTSradar outputs one of the following three alarms: 'non-UAV', 'possible UAV' and 'confirmed UAV', for a scan at a time. Since the 'possible UAV' alarm may or may not contain echo from UAVs, we compute three sets of classification accuracies for the COTSradar as follows:

- Case I: The 'Possible UAV' alarm is treated to be in the UAV category.
- Case II: The 'Possible UAV' alarm is treated to be in the non-UAV category.
- Case III: The 'Possible UAV' alarm followed by the 'Confirmed UAV' alarm is treated in the UAV category.

Test classification accuracies of the proposed system obtained at $r = 2$ and ('Yes', 'Yes'), and the COTSradar classification system are shown in Table 9. It is observed from the table that the proposed system produces 5.46–6.85% higher accuracy values than that of the COTSradar under the 2-category classification problem. The proposed system achieves about 90% of accuracy under the 3-category problem which seems reasonable.

Table 9: Test UAV classification accuracy (%) comparison between the proposed system and the COTSradar classification system. Note that the COTSradar can classify a detected target into either UAV or non-UAV only.

Number of target class	COTSradar			Proposed system
	Case I	Case II	Case III	
2 class	88.93	87.54	88.27	94.39
3 class	N.A.	N.A.	N.A.	90.59

To have a better understanding about the obtained accuracy values, both systems are now analyzed in terms of the confusion matrix as shown in Tables 10 and 11. As shown in Table 10, the proposed system achieves about 94% of correct classification rate for both non-UAV and UAV categories. However, except for the non-UAV category, the COTSradar produces about 80–88% of correct classification rate for the UAV category over all the three cases. Lastly, Table 12 shows a confusion matrix of the proposed system for the 3-category classification problem. The proposed system achieves at least about 85% of correct classification rate.

Table 10: Confusion matrix of the proposed UAV classification system obtained at $r = 2$ and ('Yes', 'Yes') under the 2-category classification problem.

		Classification output	
		Non-UAV	UAV
Truth	Non-UAV	**2,550 (93.68%)**	172 (6.32%)
	UAV	167 (5.03%)	**3,155 (94.97%)**

Table 11: Confusion matrices of the COTSradar classification function obtained under the 2-category classification problem.

		Classification output	
		Non-UAV	UAV
Truth (Case I)	Non-UAV	**2,447 (89.9%)**	275 (10.1%)
	UAV	394 (11.86%)	**2,928 (88.14%)**
Truth (Case II)	Non-UAV	**2,626 (96.47%)**	96 (3.53%)
	UAV	657 (19.78%)	**2,665 (80.22%)**
Truth (Case III)	Non-UAV	**2,588 (95.08%)**	134 (4.92%)
	UAV	575 (17.31%)	**2,747 (82.69%)**

Table 12: Confusion matrix of the proposed UAV classification system obtained at $r = 2$ and ('Yes', 'Yes') under the 3-category classification problem.

		Classification output		
		Non-UAV	Fixed-wing UAV	Rotary-wing UAV
Truth	Non-UAV	**2,490 (91.48%)**	88 (3.23%)	144 (5.29%)
	Fixed-wing UAV	90 (7.51%)	**1025 (85.56%)**	83 (6.93%)
	Rotary-wing UAV	136 (6.4%)	28 (1.32%)	**1,960 (92.28%)**

6.7. Summary of results and observations

The obtained results and observations are summarized as follows:

- The proposed UAV classification system produced 94.39% of accuracy under the 2-category (non-UAV vs. UAV) classification problem, which was 5.46−6.85% higher than that of the COTSradar classification system. Under the 3-category (non-UAV vs. fixed-wing UAV vs. rotary-wing UAV) classification problem, our system achieved 90.59% accuracy. The COTSradar classification system had no function for the 3-category classification.
- The proposed EMD-based m-DS analysis has appeared to be a promising resolution to process the 64-dimensional FMCW radar signals. Particularly, the 13 features extracted from IMFs together with the TERRM classifier were observed to possess discriminative information for UAV classification.
- The proposed rule-based scan pruning and scan-to-scan filtering functions were observed to play important roles in enhancing the classification accuracy of the proposed system. Particularly, the impact of the latter function was observed significant towards achieving a high classification accuracy.
- The TERRM classifier adopted in our system for UAV classification, was empirically shown to be much more efficient than that of the SVM classifier while producing comparable classification accuracies.

7. Conclusion

In this paper, an effective and efficient UAV classification system based on FMCW surveillance radar echo signals was proposed. The system consisted of five main parts namely, burst selection, rule-based scan pruning, extraction of features from IMFs obtained by the EMD method, TER-based classification and scan-to-scan filtering. Our experimental results obtained on physically measured FMCW radar returns from fixed-wing UAVs, rotary-wing UAVs and non-UAV objects, showed that the extracted features from IMFs contained discriminative information about targets for classification. The classification accuracy was enhanced by the proposed rule-based scan pruning and scan-to-scan filtering functions. The results also revealed that the proposed system consistently outperformed the commercial-off-the-shelf UAV classification system in terms of the classification accuracy.

Acknowledgement

The authors are thankful to the associate editor and the anonymous reviewers for their constructive and insightful comments to improve the manuscript. The authors would also like to thank Fangyuan Wan and Fengxia Wang for their efforts in radar data collection and pre-processing.

Authors Contribution Statement

- Beom-Seok Oh: Conceptualization, Investigation, Methodology, Software, Validation, Writing original draft
- Guo Xin: Data curation, Investigation, Software on radar signal processing

- Zhiping Lin: Conceptualization, Supervision, Writing review & editing

References

Al-Kaff, A., Martín, D., García, F., de la Escalera, A., & Armingol, J. M. (2018). Survey of computer vision algorithms and applications for unmanned aerial vehicles. *Expert Systems with Applications*, *92*, 447–463.

Aydın, S., Saraoğlu, H. M., & Kara, S. (2009). Log energy entropy-based EEG classification with multilayer neural networks in seizure. *Annals of biomedical engineering*, *37*, 2626–2630.

Bai, X., Xing, M., Zhou, F., Lu, G., & Bao, Z. (2008). Imaging of Micromotion Targets With Rotating Parts Based on Empirical-Mode Decomposition. *IEEE Transactions on Geoscience and Remote Sensing*, *46*, 3514–3523.

Björklund, S., Johansson, T., & Petersson, H. (2012). Evaluation of a micro-Doppler classification method on mm-wave data. In *IEEE Radar Conference* (pp. 934–939). Atlanta, GA, USA: IEEE.

Chen, V. C., & Ling, H. (2001). *Time-Frequency Transforms for Radar Imaging and Signal Analysis*. Artech House.

Du, L., Wang, B., Li, Y., & Hongwei (2013). Robust Classification Scheme for Airplane Targets With Low Resolution Radar Based on EMD-CLEAN Feature Extraction Method. *IEEE Sensors Journal*, *13*, 4648–4662.

Duda, R. O., Hart, P. E., & Stork, D. G. (2012). *Pattern Classification*. John Wiley & Sons.

Flandrin, P., & Rioul, O. (1990). Affine smoothing of the Wigner-Ville distribution. In *International Conference on Acoustics, Speech, and Signal Processing* (pp. 2455–2458). Albuquerque, New Mexico, USA.

Fleureau, J., Kachenoura, A., Albera, L., Nunes, J.-C., & Senhadji, L. (2011). Multivariate empirical mode decomposition and application to multichannel filtering. *Signal Processing*, *91*, 2783–2792.

Furlaneto, D. C., Oliveira, L. S., Menotti, D., & Cavalcanti, G. D. C. (2017). Bias effect on predicting market trends with EMD. *Expert Systems with Applications*, *82*, 19–26.

Gaur, P., Pachori, R. B., Wang, H., & Prasad, G. (2018). A multi-class EEG-based BCI classification using multivariate empirical mode decomposition based filtering and Riemannian geometry. *Expert Systems with Applications*, *95*, 201–211.

Harmanny, R. I. A., de Wit, J. J. M., & Premel-Cabic, G. (2015). Radar micro-Doppler mini-UAV classification using spectrograms and cepstrograms. *International Journal of Microwave and Wireless Technologies*, *7*, 469–477.

Huang, N. E., Shen, Z., Long, S. R., Wu, M. C., Shih, H. H., Zheng, Q., Yen, N.-C., Tung, C. C., & Liu, H. H. (1998). The empirical mode decomposition and the Hilbert spectrum for nonlinear and non-stationary time series analysis. *Proceedings of the Royal Society of London A: Mathematical, Physical and Engineering Sciences*, *454*, 903–995.

Kim, B. K., Kang, H.-S., & Park, S.-O. (2017). Drone Classification Using Convolutional Neural Networks With Merged Doppler Images. *IEEE Geoscience and Remote Sensing Letters*, *14*, 38–42.

Kim, K.-T., Seo, D.-K., & Kim, H.-T. (2002). Efficient radar target recognition using the MUSIC algorithm and invariant features. *IEEE Transactions on Antennas and Propagation*, *50*, 325–337.

Li, Y., Du, L., & Liu, H. (2013). Hierarchical Classification of Moving Vehicles Based on Empirical Mode Decomposition of Micro-Doppler Signatures. *IEEE Transactions on Geoscience and Remote Sensing*, *51*, 3001–3013.

Li, Y., Peng, Z., & Li, C. (2017). Potential active shooter detection using a portable radar sensor with micro-Doppler and range-Doppler analysis. In *Applied Computational Electromagnetics Society Symposium in China* (pp. 1–2). Suzhou, China: IEEE.

Li, Y., Peng, Z., Pal, R., & Li, C. (2019). Potential Active Shooter Detection Based on Radar Micro-Doppler and Range-Doppler Analysis Using Artificial Neural Network. *IEEE Sensors Journal*, *19*, 1052–1063.

Ma, X., Oh, B.-S., Sun, L., Toh, K.-A., & Lin, Z. (2018). EMD-based Entropy Features for micro-Doppler mini-UAV classification. In *IAPR International Conference on Pattern Recognition* (pp. 1–6). Beijing, China: IAPR.

Molchanov, P., Egiazarian, K., Astola, J., Totsky, A., Leshchenko, S., & Jarabo-Amores, M. P. (2014a). Classification of Aircraft Using Micro-Doppler Bicoherence-Based Features. *IEEE Transactions on Aerospace and Electronic Systems*, *50*, 1455–1466.

Molchanov, P., Harmanny, R. I. A., de Wit, J. J. M., Egiazarian, K., & Astola, J. (2014b). Classification of small UAVs and birds by micro-Doppler signatures. *International Journal of Microwave and Wireless Technologies*, *6*, 435–444.

Oh, B.-S., Guo, X., Wan, F., Toh, K.-A., & Lin, Z. (2017). An EMD-based micro-Doppler signature analysis for

mini-UAV blade flash reconstruction. In *22nd International Conference on Digital Signal Processing* (pp. 1–5). London, UK: IEEE.

Oh, B.-S., Guo, X., Wan, F., Toh, K.-A., & Lin, Z. (2018). Micro-Doppler Mini-UAV Classification Using Empirical-Mode Decomposition Features. *IEEE Geoscience and Remote Sensing Letters*, *15*, 227–231.

Oh, B.-S., Zhuang, H., Toh, K.-A., & Lin, Z. (2019). Augmented Empirical Mode Decomposition for Complex-Valued Univariate Signals. doi:10.1049/iet-spr.2018.5428 published online.

Ren, J., & Jiang, X. (2017). Regularized 2-D complex-log spectral analysis and subspace reliability analysis of micro-Doppler signature for UAV detection. *Pattern Recogntion*, *69*, 225–237.

Schmidt, R. (1986). Multiple emitter location and signal parameter estimation. *IEEE transactions on antennas and propagation*, *34*, 276–280.

Stankovic, L., Dakovic, M., & Thayaparan, T. (2014). *Time-frequency signal analysis with applications*. Artech house.

Stankovic, L., Djurovic, I., & Thayaparan, T. (2006a). Separation of target rigid body and micro-Doppler effects in ISAR imaging. *IEEE Transactions on Aerospace and Electronic Systems*, *42*, 1496–1506.

Stankovic, L., Thayaparan, T., & Dakovic, M. (2006b). Signal decomposition by using the S-method with application to the analysis of HF radar signals in sea-clutter. *IEEE Transactions on Signal Processing*, *54*, 4332–4342.

Sun, H., Oh, B.-S., Guo, X., & Lin, Z. (2019). Improving the Doppler Resolution of Ground-Based Surveillance Radar for Drone Detection. doi:10.1109/TAES.2019.2895585 published online.

Tahmoush, D. (2014). Detection of small UAV helicopters using micro-Doppler. In *SPIE Defense+ Security* (pp. 907717–907717). Baltimore, Maryland, USA: International Society for Optics and Photonics.

Tan, R., Lim, H. S., Smits, A. B., Harmanny, R. I. A., & Cifola, L. (2016). Improved Micro-Doppler Features Extraction Using Smoothed-Pseudo Wigner-Ville Distribution. In *IEEE Region 10 Conference* (pp. 730–733). Singapore: IEEE.

Thayaparan, T., Abrol, S., Riseborough, E., Stankovic, L. J., Lamothe, D., & Duff, G. (2007). Analysis of radar micro-Doppler signatures from experimental helicopter and human data. *Radar, Sonar & Navigation, IET*, *1*, 289–299.

The MathWorks (2019). MATLAB. `http://www.mathworks.com/`. [Online; accessed 10-February-2019].

Toh, K.-A. (2008). Deterministic neural classification. *Neural Computation*, *20*, 1565–1595.

Toh, K.-A., & Eng, H.-L. (2008). Between Classification-Error Approximation and Weighted Least-Squares Learning. *IEEE Transactions on Pattern Analysis and Machine Intelligence*, *30*, 658–669.

Toh, K.-A., Tran, Q.-L., & Srinivasan, D. (2004). Benchmarking a Reduced Multivariate Polynomial Pattern Classifier. *IEEE Transactions on Pattern Analysis and Machine Intelligence*, *26*, 740–755.

Torvik, B., Olsen, K. E., & Griffiths, H. (2016). Classification of Birds and UAVs Based on Radar Polarimetry. *IEEE Geoscience and Remote Sensing Letters*, *13*, 1305–1309.

Wang, Y., Wu, X., Li, W., Li, Z., Zhang, Y., & Zhou, J. (2016). Analysis of micro-Doppler signatures of vibration targets using EMD and SPWVD. *Neurocomputing*, *171*, 48–56.

de Wit, J. J. M., Harmanny, R. I. A., & Premel-Cabic, G. (2012). Micro-Doppler analysis of small UAVs. In *Proceedings of the 9th European Radar Conference* (pp. 210–213). Amsterdam, Netherlands: IEEE.

Wu, J.-D., & Tsai, Y.-J. (2011). Speaker identification system using empirical mode decomposition and an artificial neural network. *Expert Systems with Applications*, *38*, 6112–6117.

Yardibi, T., Li, J., Stoica, P., Xue, M., & Baggeroer, A. B. (2010). Source localization and sensing: A nonparametric iterative adaptive approach based on weighted least squares. *IEEE Transactions on Aerospace and Electronic Systems*, *46*, 425–443.

Yu, Y., Dejie, Y., & Junsheng, C. (2006). A roller bearing fault diagnosis method based on EMD energy entropy and ANN. *Journal of sound and vibration*, *294*, 269–277.

Zhou, F., Zhou, H.-M., Yang, Z., & Yang, L. (2019). EMD2FNN: A strategy combining empirical mode decomposition and factorization machine based neural network for stock market trend prediction. *Expert Systems with Applications*, *115*, 136–151.